Supplementary Information

Microstructural Origin of Selective Water Oxidation to Hydrogen Peroxide at Low Overpotentials: A Study on Mn-alloyed TiO_2

Devan Solanki‡,[1,2] Jiahui Li ‡,[1,2,3] Qianhong Zhu,[1] Xin Shen,[1,2] Grace Callander,[1,2] Jaehong Kim,[1] Yao Gang Li,[3] Hongzhi Wang,[3*] and Shu Hu [1,2*]

[1] *Department of Chemical and Environmental Engineering, Yale University, New Haven, Connecticut 06520, United States*

[2] *Energy Sciences Institute, Yale University, 810 West Campus Drive, West Haven, Connecticut 06516, United States*

[3] *State Key Laboratory for Modification of Chemical Fibers and Polymer Materials, College of Materials Science and Engineering, Donghua University, Shanghai 201620, People's Republic of China.*

‡ Jiahui Li and Devan Solanki contributed equally.

*Email: shu.hu@yale.edu; wanghz@dhu.edu.cn;

S1 Experimental Details

S1.1 Chemical and materials

All chemicals were used as received without any further purification. Tetrakis-dimethylamido-titanium (TDMAT, Sigma-Aldrich, 99.999%) and bis-(ethyl-cyclopentadienyl) manganese ($Mn(EtCp)_2$, Strem Chemicals, 99.999%) precursors for ALD were used as the Ti and Mn sources, respectively. Phosphoric acid (H_3PO_4, 85 wt % in H_2O), potassium phosphate monobasic (KH_2PO_4, ⩾98%), and potassium phosphate dibasic (K_2HPO_4, ⩾ 98%) were purchased from Sigma-Aldrich. H_2O was obtained from a Millipore deionized water system with a resistivity of 18.0 MΩ·cm. Standard titration potassium permanganate (0.1 N, $KMnO_4$, >98%) solution was purchased from Alfa-Aesar, Cerium(IV) sulfate tetrahydrate ($Ce(SO_4)_2{\cdot}4H_2O$, ⩾98%), sulfuric acid (1.0 M, H_2SO_4, 99.9%), and hydrogen peroxide (H_2O_2, 30% w/w) was purchased from Sigma-Aldrich. H_2O_2 test strips were purchased from Indigo Instruments.

S1.2 (Ti,Mn)O_x coating growth, annealing, and electrode fabrication

All catalytic films including (Ti,Mn)O_x, TiO_x, and MnO_x in this study were coated onto both fused silica (denoted as quartz interchangeably) and fluorine-doped tin oxide (denoted as FTO) substrates by using an Ultratech Fiji G2 ALD system. The reaction chamber was kept at 150 °C with an Ar (99.9997%) flow of 60 sccm in the delivery line. Films grown on quartz were used for structural and properties characterizations. The film surfaces were smooth to warrant XPS and UPS measurement to properly yield electronic structure data. **Figure S1** showed the columnar structure for a range of compositions including 4:1 and 16:1 (Ti,Mn)O_x. The grains from conformal growth coalescence to form a thin-film coating without detectable pinholes. Films grown on FTO were used for electrode fabrication, electrochemical performance measurements, and H_2O_2 quantification. Prior to ALD deposition, the FTO substrates were sonicated in ethanol for 30 minutes, dried under an N_2 flow, and loaded immediately into the ALD chamber. The general strategy of growing (Ti,Mn)O_x alloy was to deposit 2, 4, 8, and 16 cycles of TiO_2 per one cycle of MnO_x in the middle of the TiO_2 cycles. The compositions of (Ti,Mn)O_x films were controlled during ALD by varying the number of TiO_2 subcycles (2,4,8, and 16 cycles) per one MnO_x subcycle in a (Ti,Mn)O_x supercycle. Mn subcycles were placed in the midpoint within one supercycle sequence, which was then repeated to achieve the desired thickness of ca. 50 nm. This nominal ratio is correlated with but not equal to the elemental composition. For example, 2:1 TiO_2: MnO_x cycle numbers do not mean 33% Mn atomic percentage in a mixture of Mn and Ti atoms, but 54.3% Mn, which is defined as the atomic ratio of Mn%/(Mn%+Ti%) in the alloy film. The measured Mn atomic % was consistent with the previous publication.[1] The thickness of all the (Ti,Mn)O_x films was designed for 50 nm. These 50-nm thick films were sufficiently conductive for (Ti,Mn)O_x to serve as electrocatalysts, and sufficiently thick to fulfil the band diagrams as shown in **Figure 5**. After their growth, all bulk (Ti,Mn)O_x films studied were annealed in air at 500 °C for two hours. The

temperature increased with a 4 $^{o}C \cdot min^{-1}$ ramp rate, and then cooled down without active cooling. Annealing led to crystallization, with interdiffusion of Mn atoms and subsequent ripening of MnO_x crystallites. But annealing did not change the surface composition of $(Ti,Mn)O_x$ films (see **Figure S3 & Table S1**). As the control, pure TiO_2 and MnO films were deposited by ALD and then air annealed. After being annealed in air at 500 ^{o}C for two hours, crystalline TiO_2 and Mn_2O_3 were obtained. Indium (In) ohmic contacts were soldered onto the exposed FTO surfaces and formed ohmic contacts to bulk $(Ti,Mn)O_x$ films. The In contacts were then attached to coiled tin-plated Cu wires using Ag paste. The Cu wire was threaded through a glass tube, and the samples were encapsulated and sealed to the tube end using epoxy (Hysol 9460F). An optical scanner was used to image the exposed electrode, and ImageJ (open-source software made available by NIH) was used to calculate the electrode area.

S1.3 Characterizations

X-ray photoelectron spectroscopy (XPS) and ultraviolet photoelectron spectroscopy (UPS) measurements were taken with a PHI VersaProbe II Scanning XPS Microprobe. XPS characterized the compositions and electronic structures of the annealed $(Ti,Mn)O_x$ films. The elemental spectra of O 1s, C 1s, Mn 2p, Mn 3s, and Ti 2p, and the valence spectra were measured. For XPS valence band measurements, all the $(Ti,Mn)O_x$ samples were in an excellent ohmic contact with the sample holder, and the sputter-cleaned gold foil was used as a reference to calibrate the binding energy positions. The take-off angles (TOA) of 5°, 15°, 25°and 35° were used for angular-resolved XPS (AR-XPS). All XPS data were then processed using the CasaXPS software. A Hitachi SU8230 UHR Cold Field Emission scanning electron microscope (SEM) was used to characterize both film thickness and surface morphology for before and after annealing. Crystallinity and phases of $(Ti,Mn)O_x$ films on quartz were identified by Grazing Incidence X-ray Diffraction (GIXRD) using a Rigaku SmartLab X-ray diffractometer equipped with high-resolution parallel beam optics. A 1.5 kW copper tube operated at 20 kV and 2 mA; and the angle (ω) of X-ray incidence was fixed at 0.24°; a 2-theta (2θ) scan was carried out from 20° to 60°. Grazing incidence for annealed TiOx was carried out at 1.5°. Plan-view transmission electron microscopy (TEM) was performed on both the annealed 2:1 and 4:1 $(Ti,Mn)O_x$ films using an FEI Tecnai Osiris operating at 200 kV, equipped with a quadrant energy-dispersive X-ray (EDX) detector.

S1.4 Electrochemical measurements

The electrochemical behaviour of $(Ti,Mn)O_x$ electrodes was measured with a three-electrode setup. A Bio-Logic S200 potentiostat system connected the $(Ti,Mn)O_x$ working electrode, an Ag/AgCl reference electrode using saturated KCl solutions, and a Ti foil as the counter electrode. The Ti counter electrode was chosen to keep consistent with a previous study.[2] A cation exchange membrane separates the $(TiMn)O_x$ and

the Ti foil electrodes to confine the H_2O_2 production in the working electrode compartment. Cyclic voltammetry was acquired with a scan rate of 20 $mV \cdot s^{-1}$.

Chronopotentiometry (CP) and chronoamperometry (CA) were used for evaluating faradaic efficiency (FE) and long-term stability in a three-electrode cell. Uncompensated electrolyte series resistance was extracted from the impedance data measured at open circuits, and then corrected for the measured electrochemical current-potential behavior. Due to these factors, the measurement error of overpotentials reported in this work is 20 mV. Electrochemical impedance spectroscopy (EIS) was employed using the same cell as those used for the cyclic voltammetry, except measured in a $Fe(CN)_6^{3-/4-}$ redox couple electrolyte; this electrolyte is an aqueous solution containing 0.2 M $K_3Fe(CN)_6$ (Fisher Scientific, 99.4%), 0.2 M $K_4Fe(CN)_6$ (Fisher Scientific, 99.4%), and 0.2 M K_2SO_4 (Sigma-Aldrich, 99.0%). Fitting the EIS data achieved the quantification of the resistance through the $(Ti,Mn)O_x$ coatings.

S1.5 H_2O_2 quantification

The generated H_2O_2 molar quantity was detected by using a combination of H_2O_2 test strips, $Ce(SO_4)_2$ titration,and $KMnO_4$ titration. HPLC was only used initially for product idenitifcation and precision verification of other quantification techniques. First, the H_2O_2 concentration is measured and calibrated by a typical cerium sulfate (e.g., $Ce(SO_4)_2$) titration method based on the Equation S1:

$$2Ce^{4+} + H_2O_2 \rightarrow 2Ce^{3+} + 2H^+ + O_2 \quad \text{(S1)}$$

where the yellow Ce^{4+} solution was reduced to a colorless Ce^{3+} solution by reacting with H_2O_2. Thus, the H_2O_2 concentration can be determined by measuring the Ce^{4+} concentration before and after the reaction by using ultraviolet-visible (UV-vis) spectroscopy.

Ce^{4+} is only soluble in acidic solutions due to its strong tendency to hydrolyze to hydroxides. Therefore, the yellow transparent 0.5 mM $Ce(SO_4)_2$ solution was prepared by dissolving 16.6 mg $Ce(SO_4)_2$ in a 100 mL solution of the high purity H_2SO_4(aq). The as-received H_2O_2 (~30%, Sigma-Aldrich) was diluted to 100, 200, 300, 400, and 500 ppm in 0.5 M phosphate buffer solutions of pH=7, and confirmed using H_2O_2 strips. The calibration curve was obtained by measuring the intensity of UV-vis absorption spectra at 316 nm (**Figure S13a**), for those 4 mL Ce^{4+} solutions after the reaction with 50 μL H_2O_2 with known concentrations. Based on the linear relationship between the UV-vis adsorption intensity and Ce^{4+} concentration, the H_2O_2 concentrations of the samples were determined. The identical absorbance obtained by using pure water and the PB solution during the titration, as shown in **Figure S13b**, also indicates the weak binding interaction. The binding of H_2O_2 to phosphate anions is sufficiently weak not to overestimate the H_2O_2 quantity, which is different from the case of carbonate anions.

During $KMnO_4$ titration, dark purple MnO_4^- will be reduced to a clear solution by H_2O_2. The reaction is presented as Equation S2:

$$2MnO_4^- + 5H_2O_2 + 6H^+ \rightarrow 2Mn^{2+} + 5O_2 + 8\,H_2O \quad \text{(S2)}$$

Therefore, the total molar quantity (n) of H_2O_2 generated can be calculated by,

$$n(H_2O_2) = \frac{5}{2} n(MnO_4^-) \quad \text{(S3)}$$

During this process, 0.5 M H_2SO_4 prepared by diluting high purity 1.0 M H_2SO_4(aq) was used as the H^+ source. Nine standard H_2O_2 solutions (0, 1, 3, 5, 10, 25, 50, 75, and 100 ppm) were prepared and tested using the standard strips. The same series of H_2O_2 standards was quantified by the $KMnO_4$ titration. Optical spectroscopy was used to determine the titration endpoint at around 525 nm for MnO_4^- characteristic absorption. The results from the $KMnO_4$ titration were consistent with the test strips, as shown in **Figure S14**. The same H_2O_2 standard solutions were quantified by the $Ce(SO_4)_2$ titration, and the results are identical to those obtained from the $KMnO_4$ titration method. It is considered that by using the titration equipment (Titrando, Metroohm AG), nanomolar of $KMnO_4$ was added incrementally into the H_2O_2 containing solution. Therefore, the $KMnO_4$ titration was validated by the $Ce(SO_4)_2$ titration, which addresses the potential over-estimation issue due to the H_2O_2 disproportion caused by the free ions of Mn^{4+} and Mn^{2+}. The $KMnO_4$ titration was mainly used for simplicity.

Faraday efficiency (FE) for H_2O_2 production, measured in percentage, can be calculated by Equation S4:

$$FE = \frac{Amount\ of\ experimentally\ generated\ H_2O_2(mol)}{Amount\ of\ theoretically\ generated\ H_2O_2(mol)} \times 100\% \quad \text{(S3)}$$

where the amount of experimentally generated H_2O_2 can be calculated by titration (Equation S2), and the amount of theoretically generated H_2O_2 can be calculated based on the measured total charge passed at the electrode, assuming a FE=100% for $2e^-$ water oxidation (Equation S4).

$$Amount\ of\ theoretically\ generated\ H_2O_2(mol) = \frac{Q\ (C)}{F\ (C/mol) \times 2} \quad \text{(S4)}$$

where Q is the charge (C) passed during electrolysis, F is the Faraday constant (96485.3 $C \cdot mol^{-1}$), 2 is for the $2e^-$ transfer process. Two pure 0.5 M PB solutions mixed with 0 and 0.02 μmol $KMnO_4$, respectively, were assigned as standard samples to define titration destination, as shown in **Figure S15a**. During a timed

series of H_2O_2 quantification, 1 mL aliquot was extracted from the H_2O_2-containing solution in the working electrode compartment, and was mixed with 1 mL H_2SO_4 (aq, 1 M) and then titrated. This procedure was repeated three times for each data point. The excess of $KMnO_4$ in the mixed solution is ca. 0.02 μmol when the titrated line of sample solutions coincides with the magenta line (**Figure S15b**) of the standard sample for titration destination. Then, the molar amount of H_2O_2 can be calculated. The spectral sensitivity allows a detection accuracy down to 0.02 μmol, which gives a measurement error of ±0.01 $mmol \cdot L^{-1}$. Finally, 1 mL pure PB solution was added to the electrolysis cell as the H_2O_2 electrolysis continued. H_2O_2 quantification was also conducted for the electrochemical cell that operated without a membrane to separate the working and counter electrodes, and the FE results were found identical.

Gas chromatography (GC) was used to quantify any O_2 that might be evolved during H_2O_2 production. The headspace of the anode cell was sealed and was connected to an automatic sampling system. A flow of Ar gas carried any evolved O_2 from the solution and headspace to the GC (SRI Instruments 8610c). The dissolved O_2 concentrations were calibrated by flowing the mixed O_2 and Ar gases of known flow rates. The O_2 peaks were calibrated according to the O_2 concentrations. During selective H_2O_2 production, little dissolved O_2 was observed in the cell for several experiments. Thus, the FE for H_2O_2 production was reported only.

S2 Supplementary Results

S2.1 Core-level XPS of bulk (Ti,Mn)O_x

The XPS measurement and spectra analysis concerned the core-level spectral regions of O1s, Ti2p, Mn2p, Mn3s, and the valence-band (VB) spectral region. First, angle-resolved XPS (AR-XPS) was employed to measure the Mn and Ti surface compositions at tilt angles of 10, 20, 30, and 35 degrees (**Figure S3**). For both annealed and as-grown 4:1 (Ti,Mn)O_x films, Mn compositions were shown to be constant with respect to the tilt angles, which indicated the uniform compositions of Ti and Mn elements within the probing depth from 0.5 to 3.9 nm for both annealed and as-grown films including annealed 4:1 (Ti,Mn)O_x. Then, regular XPS core-level spectra were measured. C1s core-level spectra were also acquired to validate the minimal surface charging. The C1s spectrum was set at 284.8 eV, and the binding energies (BEs) of the O1s, Ti 2p and Mn 3s spectra were applied with the same BE shift by using C1s as calibration. The fitting analyses for the core-level spectra of O1s, Mn2p, $Ti2p^{3/2}$, and Mn3s sates are listed in **Table S1**.

O1s, Ti2p, Mn2p and Mn3s peaks were measured to quantify the oxidation state of (Ti,Mn)O_x films, with their spectra shown in **Figure S2**. After annealing, the Ti and Mn elements were still homogeneously distributed throughout the surface into the bulk. Annealing did not vary the Mn at% surface composition,

as indicated in **Table S2**. The 4:1 (Ti,Mn)O_x O1s core-level spectrum as shown in **Figure S2a** had an intensity maximum at 529.91 eV, consistent with the reported BEs of the oxygen O1s for TiO_2 and Mn_2O_3. This spectrum can be fitted with two peaks: the major peak, O_I, at a lower binding energy that is pertinent to O^{2-} ions forming bonds to metal cations; the other broad peak, O_{II}, at a higher binding energy is related to non-stoichiometric surface oxygen atoms, which fail to bond to metal cations but grasp surface *OH groups. **Figure S2b** shows the $Ti2p^{3/2}$ and the $Ti2p^{1/2}$ core-level peaks at 458.29 eV and 464.25 eV, respectively. The $Ti2p^{3/2}$ peak BE agrees well with published data for the Ti(IV) oxidation state in TiO_2.

The $Mn2p^{3/2}$ and Mn3s peaks were used to characterize Mn oxidation states in (Ti,Mn)O_x films. The $Mn2p^{3/2}$ and $Mn2p^{1/2}$ for Mn_2O_3 compounds should range between 641–643 and 654–655 eV, respectively, as reported in the literature.[3] Shown in **Figure S2c**, the $Mn2p^{3/2}$ peaks for (Ti,Mn)O_x films of various compositions were all located at 641.1–641.3 eV. XRD was used to determine Mn oxidation states in complementary with the previous work of using multiple peaks to fit the $Mn2p^{3/2}$ spectra.[1]. In addition, the two Mn3s core-level peaks has two, multiple split components caused by coupling of the non-ionized 3s electrons with 3d valence-band electrons. The Mn 3s separation (ΔMn 3*s*, defined as the binding energy difference between Mn $3s^5$ and Mn $3s^7$) was measured to be 5.53±0.10 eV. This BE separation indicated the Mn (III) oxidation state and was consistent with the bixbyite Mn_2O_3 phase identified for annealed (Ti,Mn)O_x.

S2.2 Electrochemical surface area (ECSA) of (Ti,Mn)O_x coatings during operation

All the annealed coatings are conformal to the FTO substrates according to SEM morphology characterizations. Their electrochemically active surface area, or the roughness factor, is calculated by taking the estimated ECSA and dividing by the geometric area of the electrode. In other words, it is calculated as C_{edl}/C_s, where C_{edl} and C_s are the double layer capacitance for the coating in the pH 7 phosphate buffer and the specific capacitance, respectively. The 4:1 ratio (Ti,Mn)O_x that was annealed at 500 °C for 2 hours had a measured C_{edl} value of 0.646 mF cm^{-2}. A C_s value of 60 μF cm^{-2} was used as the common estimate for oxide surfaces. Therefore, the roughness factor was found to be 10.7.

S2.3 Valence XPS analysis for (Ti,Mn)O_x films

All valence XPS spectra were fitted with Gaussian peaks after a Shirley background subtraction. The valence XPS spectra of (Ti,Mn)O_x films also consist of these two primary peaks of pure TiO_2. In addition, The annealed 4:1 was found to comprise another set of O 2p peaks (~0.3 eV more positive than that of pure TiO_2) due to the formation of MnO_x clusters or nanocrystals. Those Mn hybridized valence levels are designated as Mn $3d^{5/2}$ and Mn $3d^{3/2}$. The valence spectra of 4:1 (Ti,Mn)O_x was thus deconvoluted into six peaks. The two primary O 2p peaks were located at 7.10 ± 0.10 eV (purple curve) and 5.00 ± 0.10 eV (green

curve), respectively. Mn $3d^{3/2}$ was located at 3.03 ± 0.10 eV, and Mn $3d^{5/2}$ was located at 1.14 ± 0.10 eV appeared in the lower binding energy region. The intermediate band center was indicated by the intensity maximum of the fitted Mn $3d^{5/2}$. The position of valence band maximum (E_{VBM}) positions was assigned as the baseline intersection with the linear fit of valence band edges (red tangent lines of O2p-π in **Figure 4a**.

The peak fitting and deconvolution indicated that the E_F was located closer to E_{IB} than E_{VBM}. The Fermi level, E_F, was approximately half-way between the TiO_2 conduction band and the top edge of Mn-impurity IBs. Hence, the mechanism of Fermi level lowering is due to electron trapping by Mn-impurity IBs, resulting in a ground state of Mn^{3+} cations. These electronic structure analyses suggested that the Mn^{3+}-impurity IB would act as the new charge-transport band that enabled electrical conduction through the film thickness without illumination. Under the applied potential in the dark, charge hops from surface intermediates through discrete states in the Mn^{3+}-impurity state IB to the back contact, forming an anodic current. By making an analogy to the VB hole transfer at photocatalysts, we reasonably consider that the Mn^{3+} IB accepts and transports electrons freely in the dark. Across the $(Ti,Mn)O_x$ film, the trapped electrons can leave a local Mn site by hopping to a nearby acceptor site. The electrons eventually get injected to the FTO back contact and then to the counter electrode, thus completing the circuit. This charge hopping mechanism is postulated based on recently reported Ti^{3+}-defect band mediated charge transport in "leaky" amorphous TiO_2.[4]

S2.4 UV-vis for $(Ti,Mn)O_x$ films

From the UV-Vis spectra of the pure TiO_2, Mn_2O_3, and composite $(Ti,Mn)O_x$ thin films presented in **Figure S9**, the absorption edges were determined, and based on them the direct band gap energies (E_g) were successfully calculated. E_g for the pure TiO_2 thin film was calculated as ∼3.4 eV and for the Mn_2O_3 ones it was ∼2.36 eV. The UV–vis spectra of the composites are close to the spectra of the TiO_2 materials and shifted a bit toward the spectra of the Mn_2O_3. This shift was well expressed for the $(Ti,Mn)O_x$ composite, where Eg was determined from 3.28 to 2.25 with atomic ratios of Mn from 17.2 % to 54.3 %. For the $(Ti,Mn)O_x$, the shift from the bare TiO_2 fibers was not minimal (*Eg* in 2:1 composite $(Ti,Mn)O_x$ is ∼2.25 eV), showing the Mn participated electronic structure building, which also consist with Valence XPS results in Figure 4.

S3 Supplementary Discussions

S3.1 Interfacial band energetics of (Ti,Mn)O_x electrocatalysts under anodic potentials

Conventionally, the potential difference from the bulk of a metallic electrode to the redox potential at its electrochemical interface is dropped across the electrochemical double layer. Unlike this metal-liquid interface, an n-type oxide semiconductor in contact with an electrocatalytic surface behaves differently: a band bending region is induced at the solid-state semiconductor side so that the potential difference across the liquid interface is mainly dropped across this band bending region of the oxide. Here the band bending in oxides is due to the positive and fixed space charge of oxygen vacancies. This band bending picture was postulated under the principle of electrostatics, and was recently validated by *in situ* measurements of electrochemical interface energetics by ambient-pressure XPS.[5] Essentially, the density of states at each side of the electrode-electrolyte interface determine the profile of potential drop across the interface. Specifically, the space charge density of a semiconductor or a metal can be smaller or larger than the volume density of the ions in electrolytes or charged species at electrochemical double layers. To generate the band bending diagram, we took the space charge density of 2.1×10^{20} cm^{-3} for the ALD-grown TiO_2, which was determined by the Mott-Schottky analysis.

Because of the sub-surface Mn-impurity intermediate band, the (Ti,Mn)O_x surfaces exhibited anodic catalytic activity for water oxidation even in the dark. In the bulk of TiO_2 or (Ti,Mn)O_x coatings, the potential of +1.8 V_{RHE} applied to the ohmic FTO contact shifted the Fermi level, E_F, from +0.29 V_{RHE} at flat band to a value of +1.8 V_{RHE}. The position-independent value of E_F is due to zero current flow. We assume the (Ti,Mn)O_x films have the same order of magnitude oxygen vacancy concentrations and space charge density, because the growth temperatures and precursor chemistry for TiO_2 and (Ti,Mn)O_x are identical. But this space charge density for TiO_2 or the TiO_2 host oxide of (Ti,Mn)O_x coatings is orders of magnitude lower than that of the charged ions at the double layer when the films are in contact with a 0.5 M phosphate buffer. Therefore, the band edge positions of the TiO_2 were drawn to "pin" to the electrolyte potentials according to TiO_2's experimental values (**Figure 5a and 5b**). We also assume that the (Ti,Mn)O_x band edge positions are identical to those of TiO_2. The electron trapping states in the bulk of ALD-grown TiO_2 originated from the native Ti^{3+} defect states, whereas the trapping states in the bulk of (Ti,Mn)O_x films originated from the Mn^{3+} impurity states. The light grey regions indicate the unfilled Ti^{3+} defect band or Mn^{3+} intermediate band.

For (Ti,Mn)O_x films, the Mn impurities in the form of Mn_2O_3 crystallites are considered p-type semiconductors of high doping; therefore, at the liquid interface, the potential drop is within the liquid. The resistivity of the Mn_2O_3 particle film is 1.2 Ohm·cm. We can only estimate the free hole concentration. We assume a mobility of 0.01 – 0.1 cm^2 $(V\ s)^{-1}$, which is typical for those oxides, and the carrier concentration

was estimated to be ca. 5×10^{21} cm^{-3}. The Mn intermediate band is "unpinned" during the range of applied potentials, according to the principle of electrostatics. As the applied potential partially depletes the TiO_2 nanocrystals, the Mn_2O_3 nanocrystallites are filled with electrons. Their Mn IB positions with respect to redox potentials shifted according to the applied potentials. Due to the nanoscale phase segregation of bixbyite Mn_2O_3 and rutile TiO_2, their band edge alignments were drawn respectively and are drawn in **Figure 4b** as one material. In a future study, the band edge position direct measurements for $(Ti,Mn)O_x$ as a function of applied potential should be conducted following the previously reported procedure.[5]

In the case of "leaky" TiO_2 (**Figure 5a**), the bottom edge of Ti^{3+} defect bands aligned at +1.58 V_{RHE}. These electronic states are not available for accepting charge from Ti-*OH intermediates (+2.27 V_{RHE}) for the charge transfer Step (1). The *J-E* behavior under the applied potentials of +1.6 – 2.6 V_{RHE} was shown in **Figure 2a** inset. However, near the TiO_2-liquid interface there remained a charge-transfer forbidden region (between +1.58 and +2.27 V_{RHE}) where none of the electronic states was made available for charge injection from Ti-*OH surface intermediates (+2.27 V_{RHE}) into the Ti^{3+}-defect band. Charge tunneling into the Ti^{3+}-defect band is neither efficient nor possible for the range of energy levels near the Ti-*OH potential level: the depth of no-state "forbidden" region immediately underneath the liquid interface is determined by the width of the space charge region (40 nm), and is calculated to be much wider than a typical tunneling width of 1 – 2 nm. Charge tunneling to the TiO_2 VB was shown for the case of degenerately n-type doped blue TiO_2 nanotubes,[6] where their strong band bending at the liquid interface reduced the tunneling width to less than 1 – 2 nm. To summarize, "leaky" amorphous TiO_2 without Mn alloying cannot make anodic charge extraction from surface intermediates such as the Ti-*OH states in the dark.

S4. Supplementary Figures and Tables

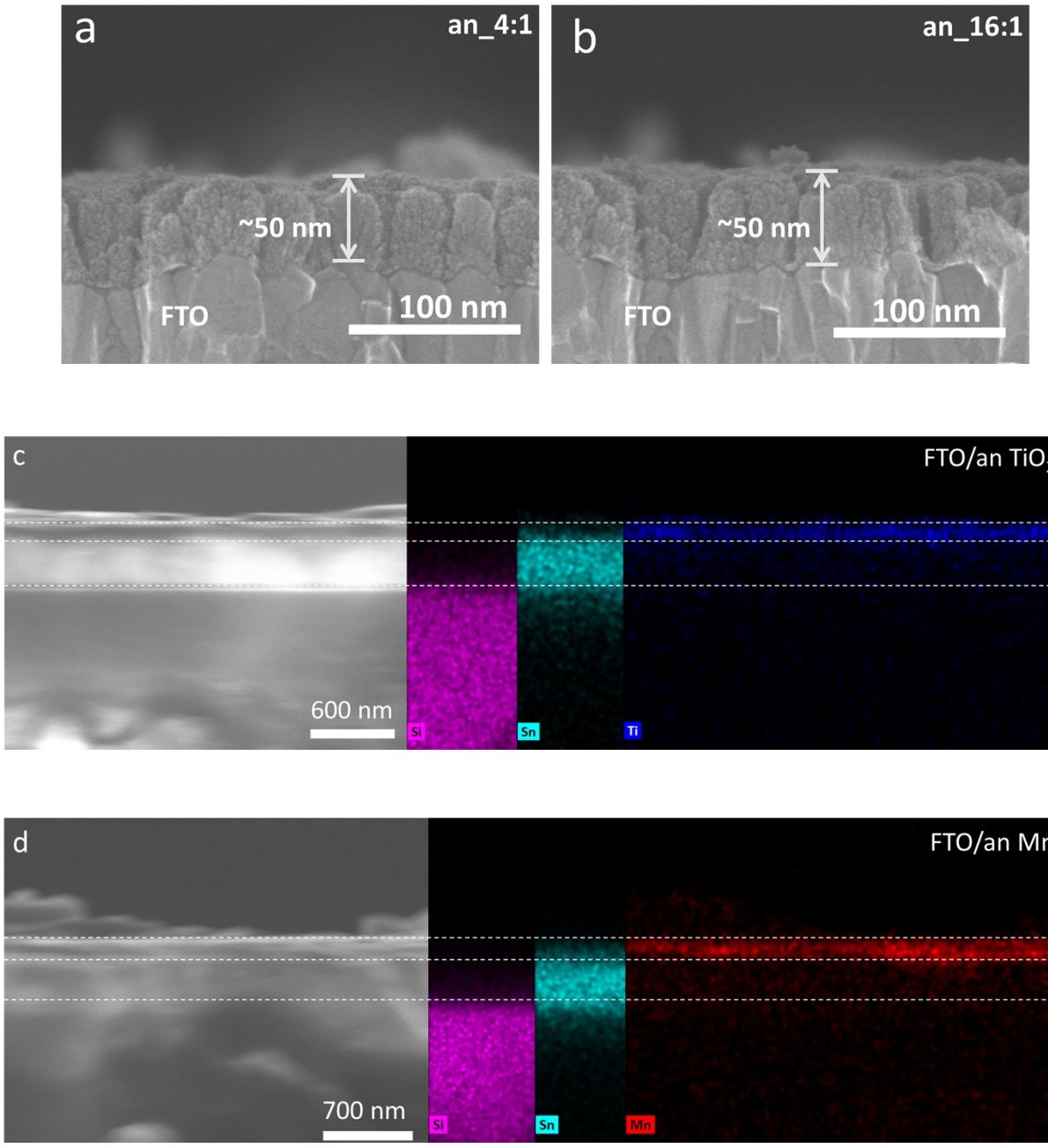

Figure S1. Cross-section SEM images of a) 4:1 $(Ti,Mn)O_x$, b) 16:1 $(Ti,Mn)O_x$, c) TiO_x, and d) MnO_x thin-film coatings on FTO substrates, after annealing in air at 500 °C for 2 hours. Dashed white lines for visualization.

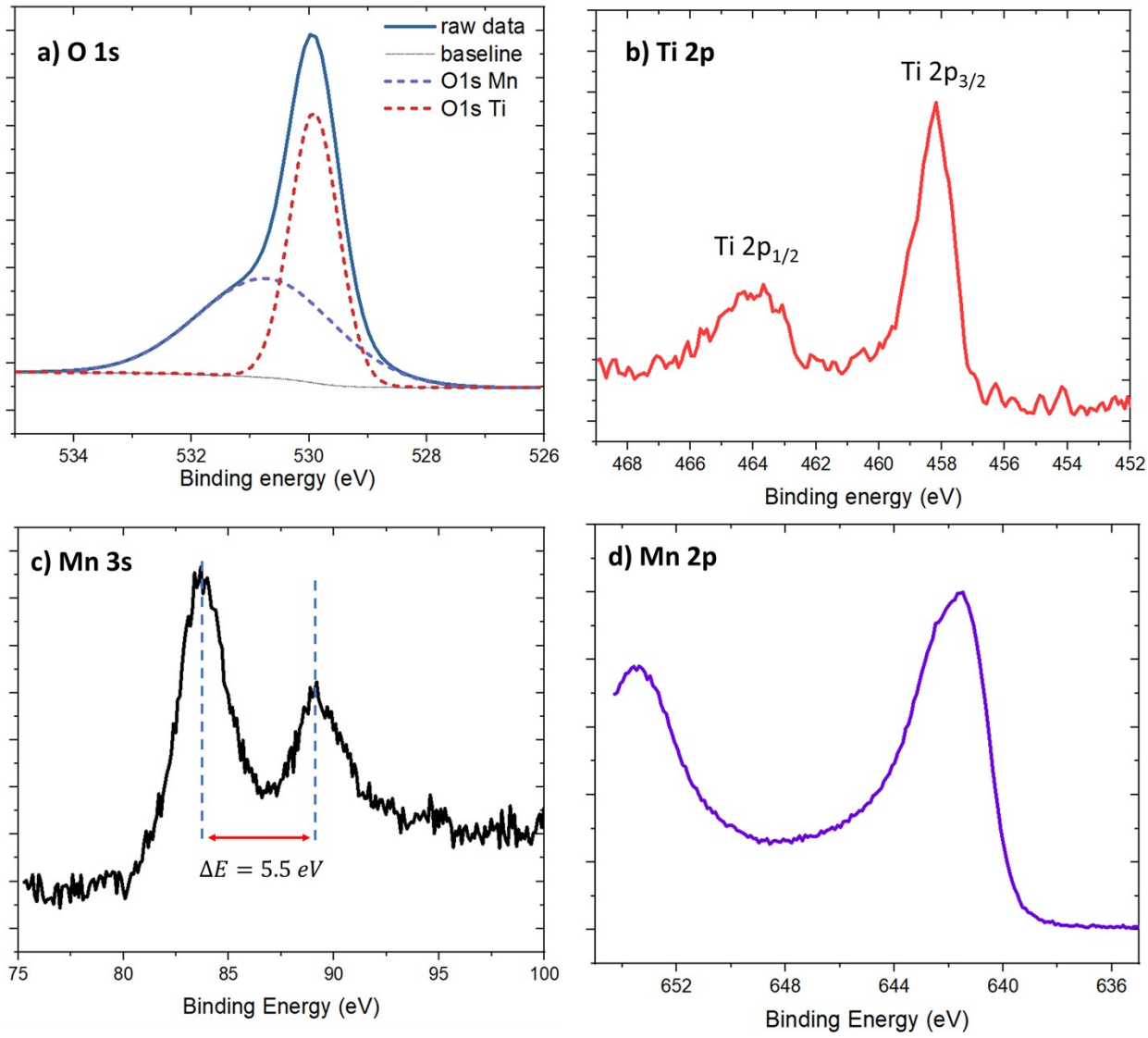

Figure S2. a) O 1s, b) Ti 2p, c) Mn 3s, and d) Mn 2p3core-level XPS spectra for the 4:1 (Ti,Mn)O_x films, which were grown on FTO substrates and then annealed in air at 500 °C for two hours.

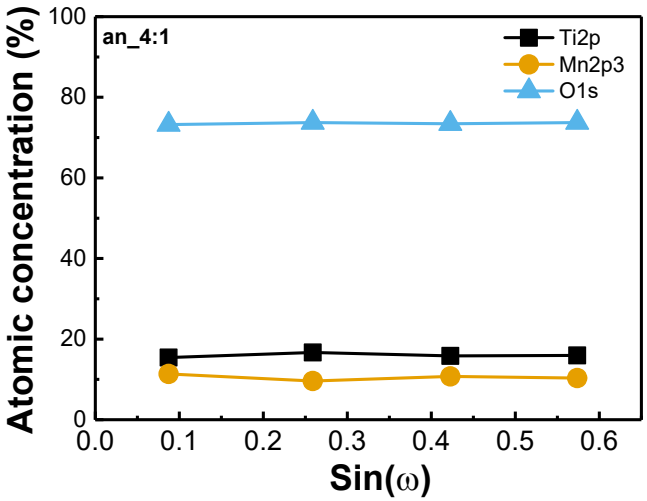

Figure S3. Correlation of the Ti, Mn and O atomic molar concentrations calculated from AR-XPS peak intensities with sin(ω), for the annealed 4:1 (Ti,Mn)O_x films, where ω is the electron "take-off angle". As ω decreased, AR-XPS measurements became more surface sensitive. This technique enables non-destructive depth profiling of Mn compositions. According to the NIST standard reference database, the inelastic mean free path of the electron from Ti 2p and Mn 2p3 is found to be 22.8 Å and 26.62 Å, respectively. The sampling depth for the (Ti,Mn)O_x surface was in the range of 6.5 – 39.1 Å for Ti, 5.6 – 33.7 Å for Mn, and 6.2 – 36.9 Å for O, as derived from the calculated electron inelastic mean free path. The Mn surface composition, i.e., Mn%/(Mn%+Ti%), was 36.09±2.1%.

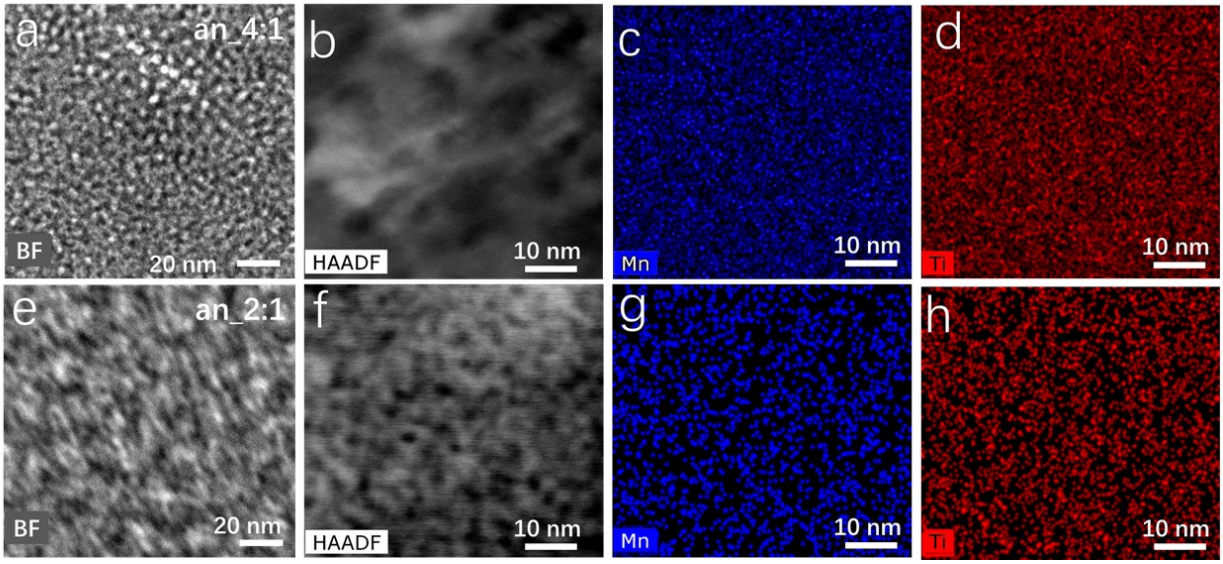

Figure S4. TEM characterizations of a-d) 4:1 and e-h) 2:1 annealed (Ti,Mn)O_x. a) and e) Bright-field TEM images, b) and f) high-angle annual dark-field STEM images, c) and g) Mn energy-dispersive x-ray (EDX) maps, and d) and h) Ti EDX maps.

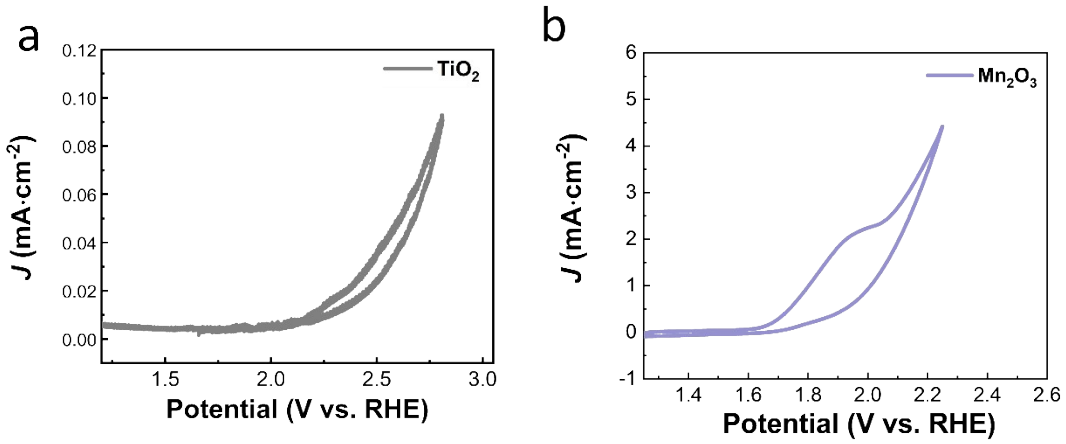

Figure S5. *J-E* behavior of (a) annealed ALD TiO_x and (b) annealed ALD MnO_x films as a blank control in 0.5 M pH = 7 phosphate buffer at a scan rate of 20 $mV \cdot s^{-1}$.

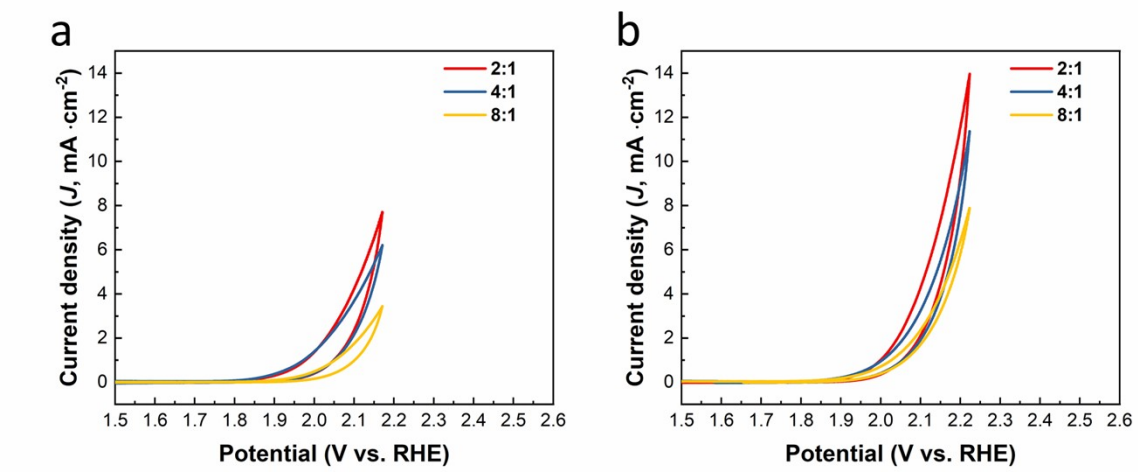

Figure S6. *J-E* curves of 500 °C air-annealed 2:1, 4:1 and 8:1 (Ti,Mn)O_x thin films measured in 0.5 M a) pH = 3, and b) pH = 9 phosphate-buffered (PB) electrolytes. The scan rate was 20 mV·s^{-1}.

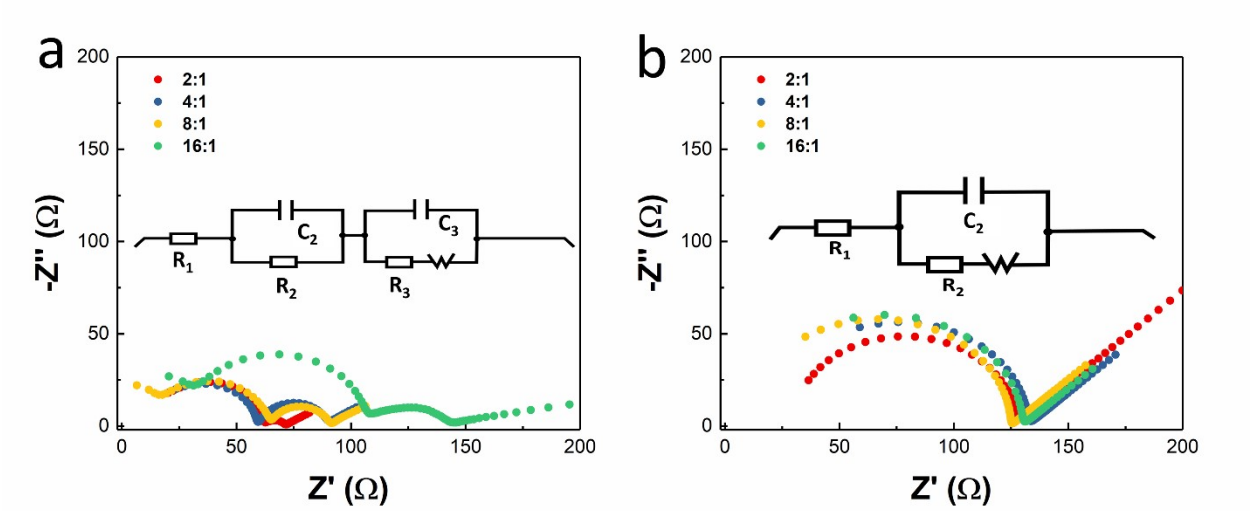

Figure S7. Electrochemical impedance profiles and resistivity analysis of annealed $(Ti,Mn)O_x$ films in contact with a) a $Fe(CN)_6^{3-/4-}$ electrolyte and b) a PB (pH = 7) electrolyte, along with the equivalent circuit models illustrated in the figure inset. Data were obtained in the frequency range from 6.0×10^6 Hz to 1.6×10^{-1} Hz. An equivalent circuitry of a series resistor in sequential connection with two pairs of parallel resistors and capacitors (constant phase elements used to justify the non-ideality of capacitance and to fit the impedance data for the $Fe(CN)_6^{3-/4-}$ electrolyte) was employed. The circuitry elements include the solution resistance (R_1); the $(Ti,Mn)O_x$ through-layer resistance (R_2) and its parallel capacitance (C_2); and the charge-transfer resistance (R_3) from $(Ti,Mn)O_x$ to the electrolyte, which is in parallel with the double layer capacitance (C_3); and the Warburg element (W) for justifying the diffusional impedance. In the PB electrolyte, only a solution resistor R_1 with through-layer resistance R_2 and its parallel capacitance C_2. The areas of all the electrodes were 0.049 cm^2.

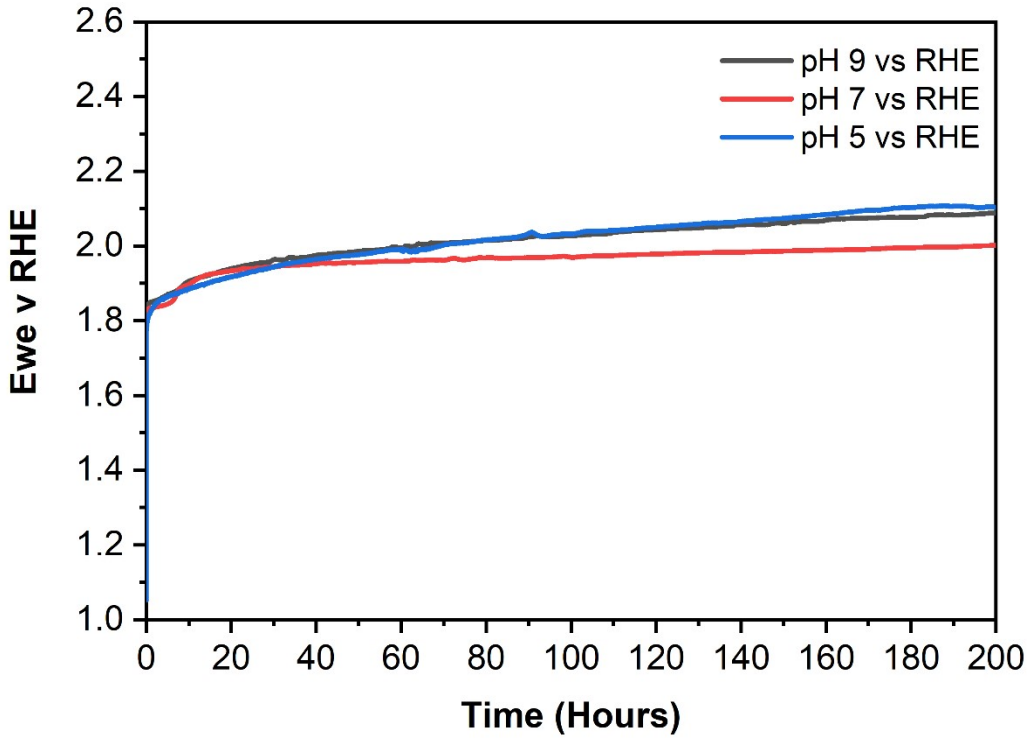

Figure S8 Chronopotentiometry(CP) measurement of the annealed 4:1 (Ti,Mn)O_x electrodes for evaluating long-term stability in 0.5M PBS solution at pH 5, 7, and 9. The current was fixed at 0.2 mA·cm^{-2}, the potentials were measured with respect to the SCE reference electrode. Ti foil was used as the counter electrode. Potentials vs SCE were converted to vs RHE by adding 0.492 V for pH 5.0, 0.667 V for pH 7.2, and 0.801 V for pH 9.5.

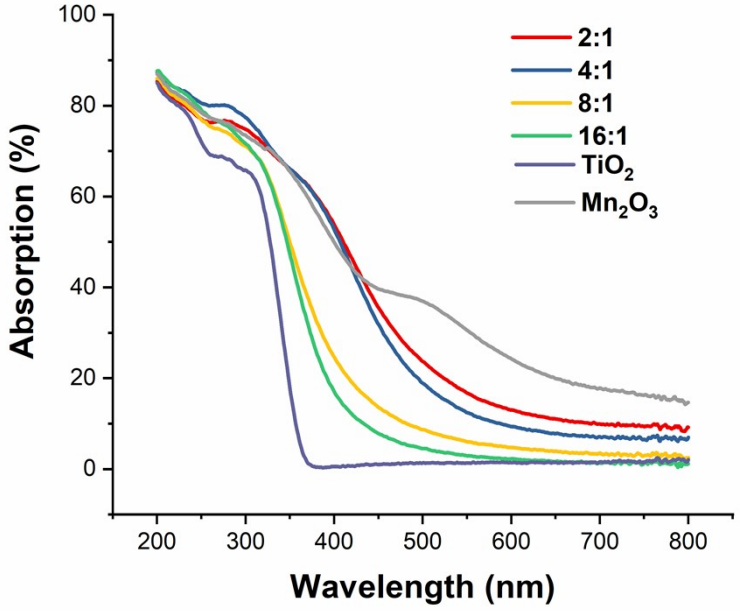

Figure S9. UV-Vis spectra of 2:1, 4:1, 8:1, 16:1 $(Ti,Mn)O_x$, and "leaky" amorphous TiO_2 and Mn_2O_3 thin films.

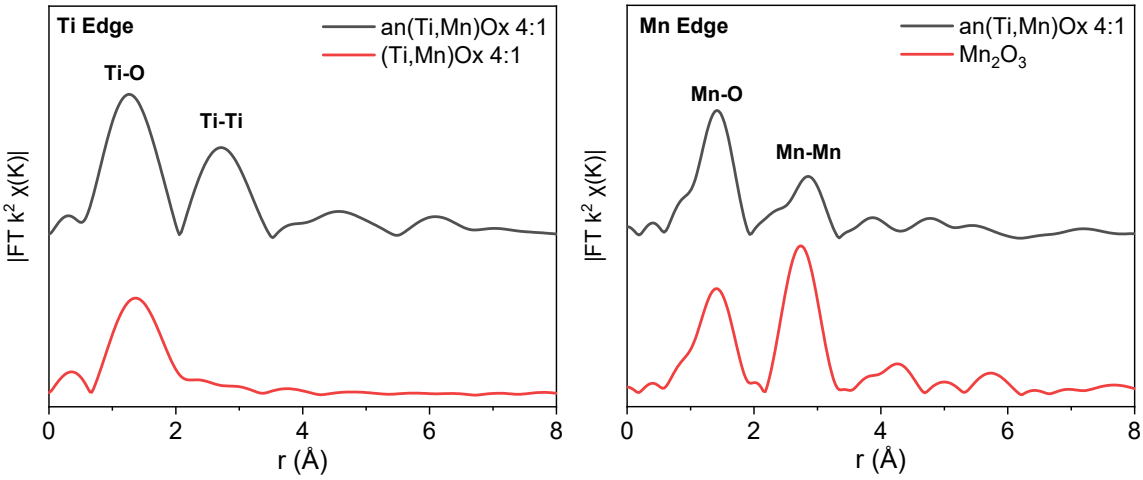

Figure S10. k^2-weighted Fourier transformed EXAFS spectra of Ti and Mn edge of annealed 4:1 $(Ti,Mn)O_x$

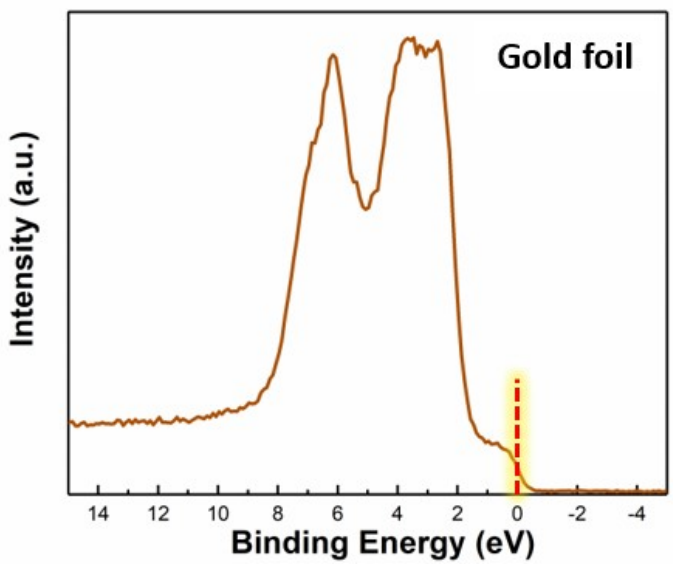

Figure S11. Valence XPS spectrum of a gold foil as a reference for the Fermi level.

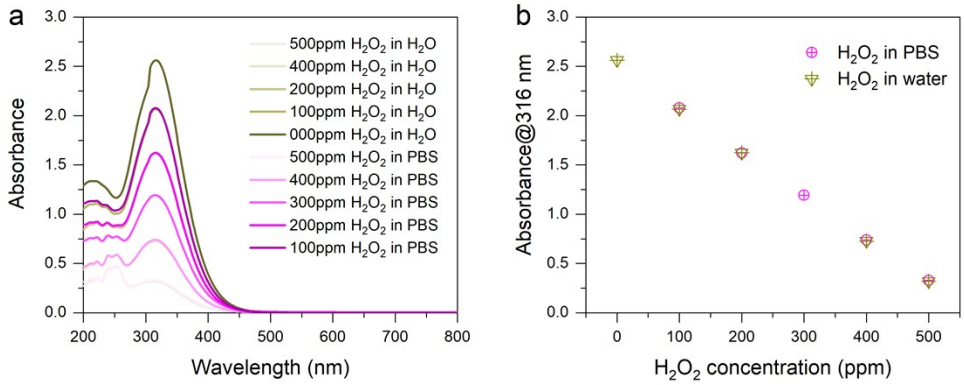

Figure S12 (a) UV-vis absorption spectra of Ce^{4+} titration by known H_2O_2 concentrations, and (b) linear fitting of absorbance at the 316 nm wavelength vs the known H_2O_2 concentrations.

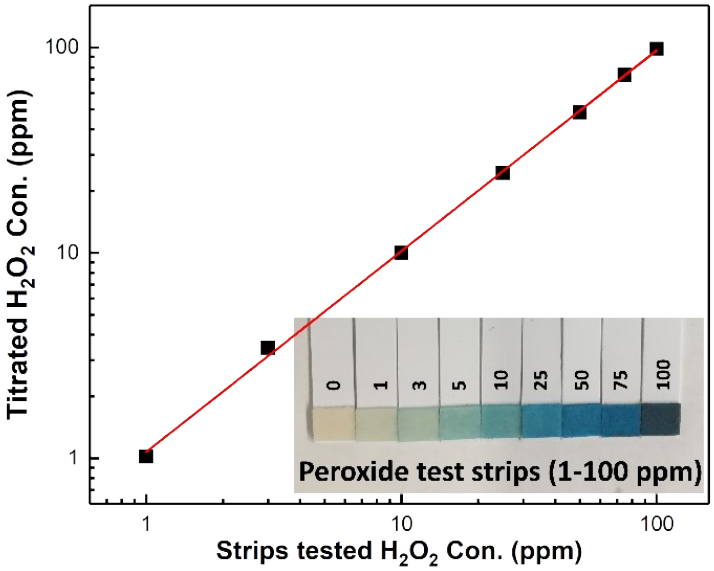

Figure S13. H_2O_2 quantification and calibration. Nine H_2O_2 aqueous standards, including the concentrations of 0, 1, 3, 5, 10, 25, 50, 75, and 100 ppm, were quantified both by using the standard strips (inset) and by using the permanganate titration.

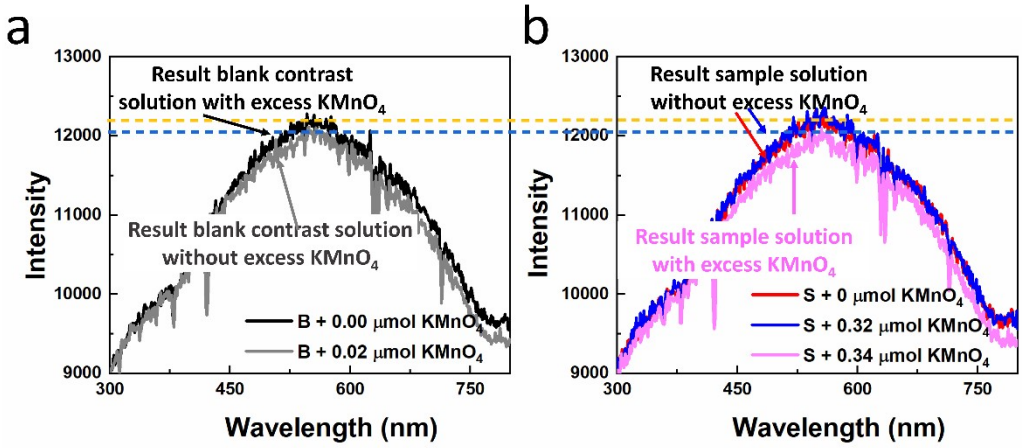

Figure S14. UV-Vis absorption spectra at 525 nm for (a) a pH=7 PB electrolyte, and (b) an H_2O_2-containing electrolysis sample solution. B refers to the blank control, a mixture of the 1 mL pH = 7 phosphate buffer and 1 mL H_2SO_4 (aq, 1.0 M) solution. S refers to a mixture of the 1 mL aliquot, which was extracted from the H_2O_2-containing electrolysis working solution, and 1 mL H_2SO_4 (aq, 1.0 M). The spectral sensitivity allows a detection accuracy down to 0.02 μmol, which gives a measurement error of 0.01 mmol L^{-1}.

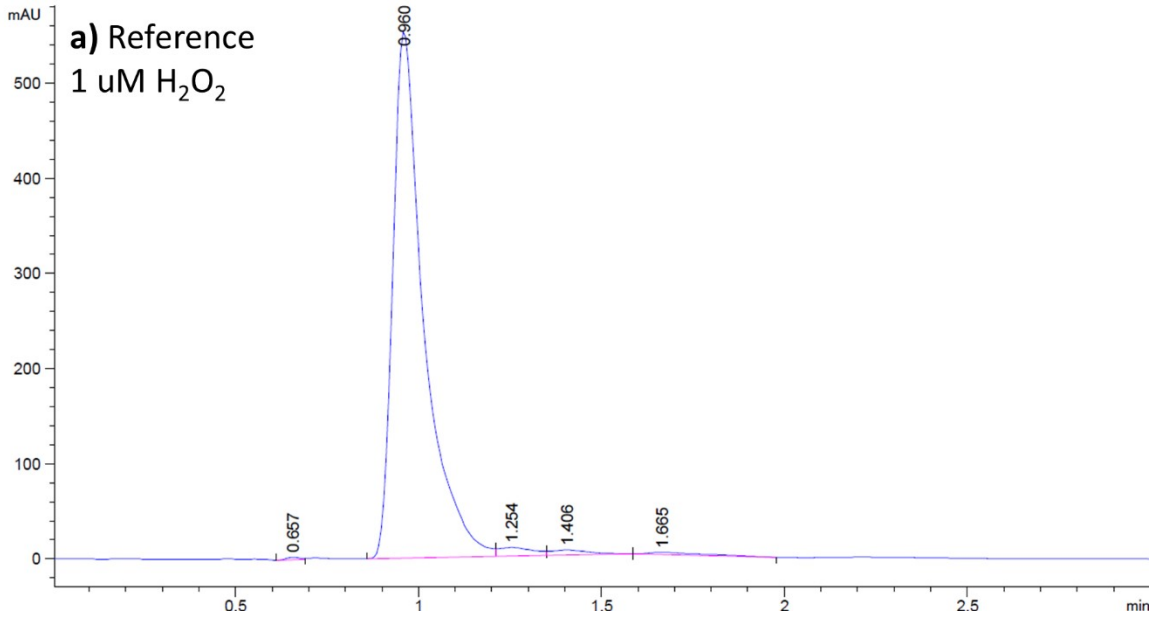

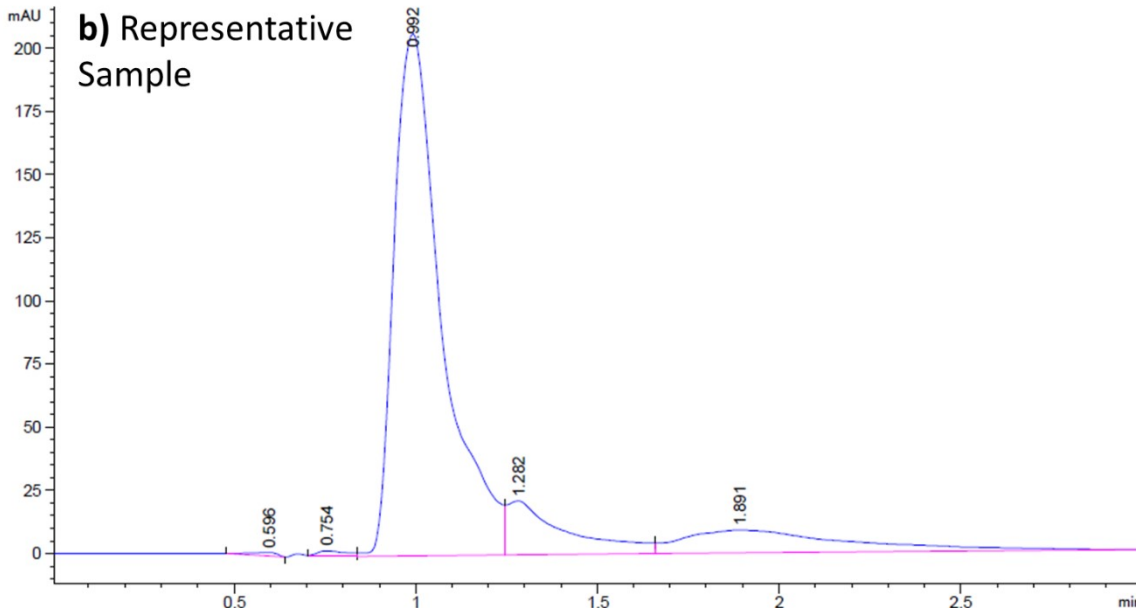

Figure S15. a) HPLC data of 1 µM H_2O_2 reference and b) HPLC data of a representative sample taken from a chronoamperometry experiment and diluted. HPLC is employed to provide the supporting evidence that the oxidant formed is molecular H_2O_2. H_2O_2 peak begins at x = .96 min. HPLC samples of 0 – 4 µM H_2O_2 are used to create a calibration curve. Using the peak area, the representative sample was determined to be .6 µM. HPLC was used strictly to verify the identity of the oxidation. Permanganate titration verified with Cerium Titration was used to quantify H_2O_2 produced. Complete data of calibration references and the three representative samples are listed in **Table S6**.

Table S1. Binding energies (BEs) and full-width at half-maxima (FWHM) of peaks in the deconvolution of $(Ti,Mn)O_x$

4:1 Annealed $(Ti,Mn)O_x$												
	Ti:Mn		$Mn3d_{5/2}$	$Mn3d_{3/2}$	O_{2p}-π (t_{2g}) From MnO_x	O_{2p}-π (t_{2g}) From TiO_2	O_{2p}-σ ($_{eg}$) From MnO_x	O_{2p}-σ ($_{eg}$) From TiO_2	E_F - E_{VBM}	E_F - E_{IB}	Mn at%	Mn at% Reported
Type 1	4-1	BE	1.14	3.03	4.30	4.85	6.80	7.10	2.31	1.14	36.09	37
		FHWM	1.60	1.85	2.14	2.15	2.20	2.28				
		A%	7.67	27.39	20.10	18.01	13.51	11.32				

Energy positions of valence band maxima and intermediate band maxima are with respect to the Fermi level positions, and Mn atomic compositions (%) of the $(Ti,Mn)O_x$ thin films that were annealed in air at 500 ºC for two hours. E_F-E_{VBM} is the difference in energy levels between the VBM and the Fermi level. The VBM is assigned by O2p-π state. E_F-E_{IB} is the difference in energy between the IB (intermediate-band position) and the Fermi level. These energy-level differences BE and FWHM are presented in the unit of eV. With XPS peak broadening effects, FWHM should make an overestimation of Mn-IB band width, or should give an upper bound for the energy range of Mn-impurity IB states. *A%* indicates the percentage area of the spectral peak's ratio that is normalized to the O2p core-level areal intensity, assigned as the *A*%s for Peaks III and IV add up to 100%. The IB centre is determined by the band position of $Mn3d^{5/2}$ states. All fitting data are listed in **Table S2** and the fitting error is ± 0.10 eV.

Table S2. Binding Energy (BE), the full wide half band-width (FWHM), and area ratios of O1s, Ti2p, Mn2p3 and Mn3s core level peaks fittings of annealed 4:1 (Ti,Mn)O_x films. BE difference between two peaks of Ti2p ($\Delta E_{Ti2p}^{1/2-3/2}$) and Mn3s ($\Delta E_{Mn\ 3s}$) were also listed. Fitting errors are ±0.02 eV.

		$O1s^{I}$ (O-OH)	$O1s^{II}$ (O-metal)	Ti2p $^{1/2}$	Ti2p $^{3/2}$	$\Delta E_{Ti2p}^{1/2-3/2}$ (±0.02 eV)	Mn2p3	ΔE_{Mn3s} (±0.01 eV)
4:1	BE (eV)	531.02	529.8	463.77	458.01	5.76	641.23	5.52
	FWHM (eV)	2.29	1.05	2.39	1.47			
	A%	36.59	63.41	34.31	65.69			

Table S3. Fitting summary for the electrochemical impedance spectroscopy (EIS) data of annealed 2:1, 4:1 8:1 and 16:1 (Ti,Mn)O_x (in air at 500 ^{o}C for 2 hours), measured in the $Fe(CN)_6^{3-/4-}$ and PB (phosphate buffer, total phosphate concentration of 0.5 M) electrolytes, respectively.

Electrolytes	$Fe(CN)_6^{3-/4-}$				PB (pH = 7, 0.5 M)			
Annealed (Ti,Mn)O_x	2-1	4-1	8-1	16-1	2-1	4-1	8-1	16-1
Solution resistance, R1 (Ω)	13.8	12.44	14.74	31.51	29.72	19.69	8.49	12.94
Through-layer resistance, R_2 (Ω)	48.6	47.25	50.02	78.02	96.84	112.3	115.8	120.3
Capacitance, C_2, ($nF \cdot cm^{-2}$)	106.3	134.3	120.4	93.9	37.45	12.18	7.35	0.96
Charge-transfer resistance, R_3 (Ω)	8.57	8.24	25.2	30.57	NA	NA	NA	NA
Double-layer capacitance, C_3 ($mF \cdot cm^{-2}$)	0.47	0.6	0.2	0.14	NA	NA	NA	NA
Diffusion coefficient ($Ohm \cdot s^{-1/2}$)	7.156	11.08	9.5	20.07	937.1	622.1	346.1	565

Table S4. Summary of the current density (J, mA·cm^{-2}) and charge quantity (Q-Q_0, C) vs. time (h), the titration outcome and the averaged Faradaic efficiency (FE).

Time (h)	Current density (J, mA·cm^{-2})	Charge (C)	Titration $KMnO_4$ (mL)	n_{H2O2} (μmol)	c_{H2O2} (mmol·L^{-1})	$n^{\theta}(H_2O_2)$ (μmol)	FE (%)
1	0.24	1.90	0.048	9.6	0.49	9.85	97.50
2	0.19	3.63	0.089	17.8	0.94	18.79	91.68
3	0.20	4.93	0.120	24.0	1.28	25.55	91.75
4	0.20	6.30	0.149	29.8	1.63	32.65	81.70
6	0.17	8.94	0.204	40.8	2.32	46.33	80.40
8	0.16	11.47	0.255	51.0	2.97	59.44	77.80

4:1(Ti,Mn)O_x film electrode (1.2 cm^2 electrode area) was used. All electrolysis measurements were conducted in 20 mL, 0.5 M, and pH = 7 PB electrolytes, with a Ti foil as the counter electrode. The FE (%) is reported for an averaged value at the time of cumulative hours. For example, the FE after eight-hour electrolysis was calculated using the total accumulated molar quantity of H_2O_2 (e.g., 59.44 μmol) divided by the total charge passed (e.g., 11.47 C) by following Equations S1– S4.

Table S5. Comparison to published work on selective water oxidation for H_2O_2 production.

H_2O_2 Generation	Sayama and co-workers			Zheng and co-workers		Wang and co-workers	This work
Catalyst (anode) [Ref]	$BiVO_4$[7]	$WO_3/BiVO_4$[8]	$WO_3/BiVO_4/Al_2O_3$[9]	$BiVO_4$[2]	$BiVO_4$[10]	Carbon fiber [11]	$(Ti,Mn)O_x$
Overpotential (mV, vs. 1.76 V_{RHE}) at J=0.2 mA cm^{-2}	500 mV	/	/	500 mV	/	/	50 mV
Highest FE (%)	35% (under illumination)	54% (under illumination)	80% (under illumination)	70% (in the dark)	95% (under illumination)	66% (in the dark)	>95% (in the dark)
Accumulated n (μmol) per Q (C)	0.76 μmol/C (220 C)	0.45 μmol/C (50 C)	0.7 μmol/C (100 C)	2.56 μmol/C (17C)	2.56 μmol/C (3C)	5.19 μmol/C (805 C)	4.82 μmol/C (11.4 C)
Average FE (%) (5.18 μmol C^{-1} for 100%)	14.8%	28%	13.5%	70%	53%	66%	93.5%
$c(H_2O_2)$ (mmol L^{-1})	5 mM (35 mL)	1.3 mM (35 mL)	2 mM (35 mL)	0.5 mM (15 mL)	5.12 mM (15 mL)	167 mM (25 mL)	2.9 mM (20 mL)

Table S6. Data from HPLC (see **Figure S15** and Ret is short for Retention)

Reference 1 (0 μM)					
Peak #	Ret Time (min)	Width	Area	Height	Area %
1	0.657	0.039	5.591	2.345	2.964
2	**0.961**	**0.091**	**142.237**	**22.317**	**71.334**
3	1.67	0.183	51.25	3.713	25.703
Reference 2 (1 μM)					
Peak #	Ret Time (min)	Width	Area	Height	Area %
1	0.657	0.404	7.37	2.828	0.218
2	**0.96**	**0.086**	**3252.686**	**553.662**	**96.057**
3	1.254	0.094	59.431	9.049	1.755
4	1.406	0.107	39.708	5.411	1.173
5	1.665	0.144	26.996	2.57	0.079
Reference 3 (2 μM)					
Peak #	Ret Time (min)	Width	Area	Height	Area %
1	0.653	0.0456	8.486	2.949	0.135
2	**0.961**	**0.0855**	**6028.245**	**1011.931**	**95.604**
3	1.253	0.0917	110.421	17.007	1.751
4	1.397	0.1068	82.406	11.071	1.307

5	1.663	0.0815	11.089	2.036	0.176
6	1.786	0.126	28.833	3.365	0.457
7	2.188	0.3148	35.976	1.819	0.571
Reference 3 (3 µM)					
Peak #	Ret Time (min)	Width	Area	Height	Area %
1	0.534	0.133	30.237	3.076	0.323
2	0.657	0.039	5.832	2.361	0.062
3	**0.96**	**0.085**	**8919.528**	**1512.307**	**95.286**
4	1.252	0.091	163.877	25.45	1.751
5	1.39	0.104	120.575	16.719	1.288
6	1.657	0.073	7.161	1.476	0.077
7	1.789	0.123	61.447	7.209	0.656
8	2.176	0.331	51.13	2.438	0.557
Reference 4 (4 µM)					
Peak #	Ret Time (min)	Width	Area	Height	Area %
1	0.532	0.1563	46.713	4.118	0.38
2	0.657	0.042	5.648	2.201	0.046
3	**0.959**	**0.087**	**11681.1**	**1963.293**	**95.058**
4	1.252	0.093	215.037	33.601	1.749
5	1.388	0.113	186.271	23.404	1.515
6	1.786	0.119	91.334	11.406	0.0743
7	2.171	0.312	62.27	2.599	0.507
Sample 1					
Peak #	Ret Time (min)	Width	Area	Height	Area %
1	0.596	0.067	6.496	1.391	0.026
2	0.754	0.081	12.624	2.262	0.515
3	**0.992**	**0.139**	**1894.459**	**206.625**	**77.304**
4	1.282	0.149	244.281	21.339	9.968
5	1.891	0.435	292.799	9.017	11.948
Sample 2					
Peak #	Ret Time (min)	Width	Area	Height	Area %
1	0.757	0.088	15.182	2.467	0.594
2	**0.992**	**0.144**	**1987.855**	**211.339**	**77.766**
3	1.277	0.152	269.227	22.751	10.532
4	1.866	0.41	283.938	8.621	11.108
Sample 3					
Peak #	Ret Time (min)	Width	Area	Height	Area %
1	0.59	0.085	10.736	1.756	0.434
2	0.754	0.088	14.861	2.417	0.601
3	**0.991**	**0.148**	**1911.921**	**199.918**	**77.234**
4	1.276	0.153	265.049	22.231	10.707
5	1.861	0.419	272.909	8.472	11.024

S5. Supplementary References

1. Siddiqi, G.; Luo, Z.; Xie, Y.; Pan, Z.; Zhu, Q.; Röhr, J. A.; Cha, J. J.; Hu, S., Stable water oxidation in acid using manganese-modified TiO_2 protective coatings. *ACS Applied Materials & Intererfaces* **2018,** *10* (22), 18805-18815.
2. Shi, X.; Siahrostami, S.; Li, G.-L.; Zhang, Y.; Chakthranont, P.; Studt, F.; Jaramillo, T. F.; Zheng, X.; Nørskov, J. K., Understanding activity trends in electrochemical water oxidation to form hydrogen peroxide. *Nature Communications* **2017,** *8* (1), 701.
3. Nelson, A.; Reynolds, J. G.; Roos, J. W., Core-level satellites and outer core-level multiplet splitting in Mn model compounds. *Journal of Vacuum Science & Technology A: Vacuum, Surfaces, and Films* **2000,** *18* (4), 1072-1076.
4. Nunez, P.; Richter, M. H.; Piercy, B. D.; Roske, C. W.; Cabán-Acevedo, M.; Losego, M. D.; Konezny, S. J.; Fermin, D. J.; Hu, S.; Brunschwig, B. S.; Lewis, N. S., Characterization of electronic transport through amorphous TiO_2 produced by atomic-layer deposition. *The Journal of Physical Chemistry C* **2019** *123 (33), 20116-20129*.
5. Lichterman, M. F.; Hu, S.; Richter, M. H.; Crumlin, E. J.; Axnanda, S.; Favaro, M.; Drisdell, W.; Hussain, Z.; Mayer, T.; Brunschwig, B. S.; Lewis, N. S.; Liu, Z.; Lewerenz, H.-J., Direct observation of the energetics at a semiconductor/liquid junction by operando X-ray photoelectron spectroscopy. *Energy & Environmental Science* **2015,** *8* (8), 2409-2416.
6. Yang, Y.; Hoffmann, M. R., Synthesis and stabilization of blue-black TiO_2 nanotube arrays for electrochemical oxidant generation and wastewater treatment. *Environmental Science & Technology* **2016,** *50* (21), 11888-11894.
7. Fuku, K.; Miyase, Y.; Miseki, Y.; Gunji, T.; Sayama, K., Enhanced oxidative hydrogen peroxide production on conducting glass anodes modified with metal oxides. *ChemistrySelect* **2016,** *1* (18), 5721-5726.
8. Fuku, K.; Miyase, Y.; Miseki, Y.; Gunji, T.; Sayama, K., WO_3/$BiVO_4$ photoanode coated with mesoporous Al_2O_3 layer for oxidative production of hydrogen peroxide from water with high selectivity. *RSC Advances* **2017,** *7* (75), 47619-47623.
9. Fuku, K.; Sayama, K., Efficient oxidative hydrogen peroxide production and accumulation in photoelectrochemical water splitting using a tungsten trioxide/bismuth vanadate photoanode. *Chemical Communications* **2016,** *52* (31), 5406-5409.
10. Shi, X.; Zhang, Y.; Siahrostami, S.; Zheng, X., Light-driven $BiVO_4$–C fuel cell with simultaneous production of H_2O_2. *Advanced Energy Materials* **2018**, 1801158.
11. Xia, C.; Back, S.; Ringe, S.; Jiang, K.; Chen, F.; Sun, X.; Siahrostami, S.; Chan, K.; Wang, H., Confined local oxygen gas promotes electrochemical water oxidation to hydrogen peroxide. *Nature Catalysis* **2020,** *3* (2), 125-134.